A 9.7-nT$_{rms}$, 704-ms Magnetic Biosensor Front-End for Detecting Magneto-Relaxation

Xiahan Zhou, *Member, IEEE*, Enhan Mai, *Student Member, IEEE*, Michael Sveiven, Corentin Pochet, *Graduate Student Member, IEEE*, Haowei Jiang, *Member, IEEE*, Chih-Cheng Huang, and Drew A. Hall, *Senior Member, IEEE*

***Abstract*—This article reports a low-noise magnetic sensor front-end with an 18-bit Zoom ADC for detecting temporal magnetic nanoparticle (MNP) relaxation. Techniques such as dynamic element matching (DEM) and magnetoresistive correlated double sampling (MRCDS) are proposed to remove the sensor and analog front-end (AFE) 1/*f* noise while a fast-settling Miller compensation (FSMC) technique is proposed to reduce the amplifier power. Collectively, these result in state-of-the-art input-referred noise performance (9.7 nT$_{rms}$) and a figure-of-merit (FoM) that is 6.6× and 210× better than previously reported magnetic sensor and relaxation-based AFEs, respectively. A relaxation-based magnetic immunoassay (MIA) was performed to demonstrate the concept. This design is implemented in a 0.18-μm CMOS process and consumes 4.32 mW from a 1.8-V supply.**

***Index Terms*—Magnetic immunoassay (MIA), magnetic sensor, relaxometry, sensor analog front-end (AFE), Zoom ADC.**

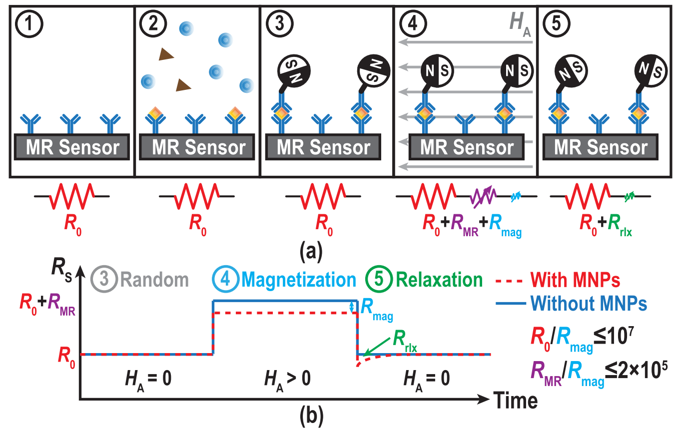

Fig. 1. (a) Illustration of an MIA where underlying MR sensors detect MNP labeled antigen-antibody complexes, and (b) transient response of an MR sensor in an MIA.

I. Introduction

POINT-OF-CARE (PoC) biomolecular testing is gaining momentum worldwide for rapidly diagnosing disease and remotely monitoring disease progression [1]–[3]. Such tests need compact, fast turn-around time, and accurate biosensors. Most PoC biosensors today are either colorimetric lateral flow immunoassays based on an enzyme-linked immunosorbent assay (ELISA) or electrochemical sensors with enzymatic assays (*e.g.*, glucometers) [4], [5]. While extremely prevalent, lateral flow assays have low sensitivity and are only semi-qualitative, typically relegating them to applications with binary outcomes (*e.g.*, pregnancy and strep throat) and high abundance biomarkers [6]. On the other hand, electrochemical sensors can be extremely sensitive and compact, but often suffer from matrix effects (*e.g.*, pH, ionic strength, and temperature) requiring sample pretreatment steps. These assays can also be sensitive to redox active interfering species [7], [8]. Thus, there remains an unmet need for highly sensitive biosensors for PoC applications.

Manuscript received August 3, 2020; revised November 5, 2020; accepted November 28, 2020. Date of publication January 6, 2021; date of current version June 29, 2021. This article was approved by Associate Editor Pui-In Mak. This work was supported in part by the National Science Foundation under Grant ECCS-1454608 and Qualcomm. *(Corresponding author: Drew A. Hall.)*

The authors are with the Department of Electrical and Computer Engineering, University of California San Diego, La Jolla, CA 92093 USA (e-mail: drewhall@ucsd.edu).

Color versions of one or more figures in this article are available at https://doi.org/10.1109/JSSC.2020.3043669.

Digital Object Identifier 10.1109/JSSC.2020.3043669

Magnetic sensors have been reported for high sensitivity biomolecular testing [9]–[17]. The high sensitivity is, in part, due to the sample matrix (*i.e.* urine, saliva, and blood) being devoid of a magnetic background enabling matrix-insensitive biomarker detection [18], [19]. The small size and CMOS compatibility make magnetic sensors attractive for PoC applications [20], [21]. Several types of magnetic sensors have been demonstrated, such as *LC* oscillator-based sensors [11], Hall-effect sensors [12], [13], and magnetoresistive (MR) sensors [14]–[17]. MR sensors were chosen for this work due to their high transduction efficiency enabling detection of nanometer-sized magnetic nanoparticles (MNPs) [19]. While the transduction method differs (*e.g.*, spin-dependent scattering versus tunneling), all MR sensors can generically be modeled as a differential resistance proportional to the magnetic field [22].

A magnetic immunoassay (MIA), a modified form of an ELISA, is used to deploy an MR sensor for biosensing, as shown in Fig. 1(a). Initially, capture antibodies are immobilized on the sensor surface (Step 1). Next, the sample is added, and the target biomarkers bind to the capture antibodies (Step 2). Then MNP-conjugated detection antibodies are added and bind to form a sandwich structure, as shown in Step 3. Since the MNPs are superparamagnetic, they have a random orientation without an applied field and exert zero net field on the underlying sensors. Thus, the MR sensor remains at its nominal resistance, R_0. During Step 4, an external magnetic

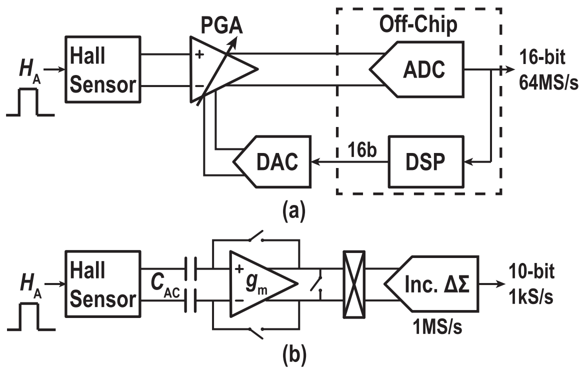

Fig. 2. Prior MRX-based AFEs. (a) Liu, JSSC 2012. (b) Gambini, JSSC 2013.

field, H_A, is applied along the sensor's short axis that polarizes the MNPs generating a stray field that is proportional to the number of tethered MNPs. The sensor resistance changes to $R_0 + R_{MR} + R_{mag}$, where R_{MR} is the magnetoresistance due to H_A and R_{mag} is the magnetoresistance signal due to the stray field from the tethered MNPs. The transient sensor response, R_S, is illustrated in Fig. 1(b). Conventional magnetometry measures R_{mag} at Step 4 to quantify the number of MNPs, which is directly proportional to the number of captured biomarkers [14]–[17]. However, the large baseline to signal ratio (R_0/R_{mag}) requires the AFE to have a dynamic range (DR) of >140 dB.

To cancel the baseline, magneto-relaxometry (MRX) was proposed to detect the temporal relaxation of the tethered MNPs rather than the static magnetization [12], [13]. Instead of measuring R_{mag} superimposed on R_0 and R_{MR} during Step 4, an additional step (Step 5) is added where H_A is rapidly removed resulting in the MNPs losing their magnetization. The MNPs return to a random state via Néel and/or Brownian relaxation. Brownian relaxation rotates the whole particle via Brownian motion [23] whereas Néel relaxation uses internal domain movement [24]. Since the MNPs are immobilized by the antibodies, Néel relaxation dominates the process [25]. The MNP magnetization as a function of time [26] can be written as

$$M_N(t) = C \cdot \ln\left(1 + \frac{t_C}{t}\right) \tag{1}$$

where t is the time after removing H_A, t_C is the characteristic time that depends on the magnetization time and applied field strength, and C is a scaling factor dependent on the surface coverage, magnetic viscosity, and initial magnetization [27]. $M_N(t)$, in units of A/m, is proportional to the number of MNPs after considering particle-to-particle interactions and the MNP size/shape distribution [27], [28]. Therefore, by measuring the temporal relaxation signal, R_{rlx}, during Step 5, the number of tethered MNPs can be quantified. Using magnetic correlated double sampling (MCDS) where the signal at Step 5 is subtracted from the signal at Step 3, the baseline can be eliminated [13], [29]. Compared to magnetometry, MRX eliminates the baseline and relaxes the H_A uniformity requirement.

A few CMOS AFEs have been reported for MRX using Hall-effect sensors. Fig. 2(a) shows an AFE with a programmable gain amplifier (PGA) and an offset cancellation loop to remove the equivalent sensor R_0 baseline [12]. An off-chip high-speed ADC captures the fast relaxation signal. In [13], an incremental $\Delta\Sigma$ ADC was used to integrate R_{rlx} during the relaxation phase, as shown in Fig. 2(b). Since R_{rlx} is the largest immediately after removing H_A and decays over time, integrating R_{rlx} at the beginning of the relaxation phase captures most of the signal, while reducing the power consumption, thus achieving high efficiency. While promising, the magnetic sensor figure-of-merit (FoM), defined as Resolution$^2 \cdot$ Energy/Conversion [30], [31], for both of these designs is 32× worse than state-of-the-art magnetometry-based AFEs. The challenges for MRX-based AFEs are: 1) MRX requires two more steps (Steps 3 and 5) leading to a 3× longer readout time and 2) the relaxation signal is broadband and overlaps with the sensor and AFE $1/f$ noise.

TABLE I
TARGET SPECIFICATIONS OF THE MAGNETIC SENSOR AFE

	State-of-the-Art [16]	Target
Sensitivity	N/A	< 0.1 ppm
Baseline	7.09 mT	< 0.3 mT
Total Noise	49 nT_{rms}	< 14.4 nT_{rms}
Readout Time	250 ms	< 1 s
Power Consumption	3.15 mW	< 5 mW

This article targets the best FoM based on MRX. Table I lists the state-of-the-art that is based on magnetometry [16] and our target specifications. A sensitivity (noise in Ω/R_0) of 0.98 parts-per-million (ppm) was reported in [17], so the target sensitivity was set to 0.1 ppm, with a comparable readout time <1 s and power consumption <5 mW. Target baseline and integrated noise are based on the sensor parameters. With $R_0 = 1.3$ kΩ, a transduction coefficient of 9 Ω/mT, and $H_A = 3$ mT, the target noise is 14.4 nT_{rms}. To have a negligible baseline, the target baseline is set to 10× smaller than H_A.

To achieve these specifications, we propose a CMOS architecture with a MR-correlated double sampling (MRCDS) technique to reduce the readout time and system $1/f$ noise. DEM in the sensor bias network shapes and filters the $1/f$ noise. A fast-settling Miller compensation (FSMC) technique in the capacitively coupled instrumentation amplifier (CCIA) is proposed to reduce the power consumption. These result in an input-referred noise of 9.7 nT_{rms}, a power consumption of 4.32 mW, a readout time of 704 ms, and an FoM of 286 $nT^2 \cdot$ mJ—6.6× and 210× better than previously reported magnetometry and MRX-based AFEs, respectively.

The rest of the article is organized as follows. Section II describes the MRCDS and the system architecture followed by the circuit implementation in Section III. Section IV shows measurement results and conclusions are drawn in Section V.

II. System Architecture

A. Magnetoresistive Correlated Double Sampling

Fig. 3(a) shows the readout timing diagram that includes Steps 3–5 with the same duration, T_{cycle}. MCDS subtracts the signal at Step 3 from the signal at Step 5 to eliminate the baseline but suffers from long readout time and poor $1/f$ noise

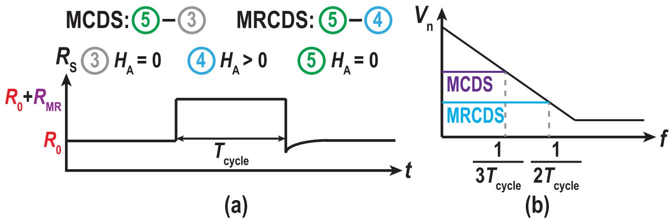

Fig. 3. Comparison of MCDS and MRCDS. (a) Signal timing diagram. (b) $1/f$ noise rejection.

TABLE II
COMPARISON OF MCDS AND MRCDS

	MCDS	MRCDS
$1/f$ noise rejection	$f < 1/(3T_{cycle})$	$f < 1/(2T_{cycle})$
Readout time	$3T_{cycle}$	$2T_{cycle}$
Total noise (same readout time)	$\sqrt{1.5} \sim 1.5\times$	$1\times$
Baseline	0	R_{MR}
Temp drift cancellation	Good	Fair
Needs reference sensor?	No	No

rejection. We propose an MRCDS technique that subtracts the signal at Step 4 from the signal at Step 5. Step 3 is no longer needed and thus the readout time is reduced. The $1/f$ noise rejection is illustrated in Fig. 3(b) assuming that the AFE $1/f$ noise corner frequency is higher than $1/(2T_{cycle})$. Due to higher correlation, $1/f$ noise that is $<1/(2T_{cycle})$ is eliminated for MRCDS while MCDS only removes $1/f$ noise that is $<1/(3T_{cycle})$. It should be noted that both techniques completely remove $1/f$ noise at low frequencies, thus enabling an unlimited tradeoff between resolution and readout time. Normalized to the same readout time considering only white noise, the noise improvement from MRCDS is $\sqrt{1.5}\times$ because of the $1.5\times$ shorter time compared to MCDS; if only $1/f$ noise is considered, the noise improvement from MRCDS is $1.5\times$ because of the $1/f$ noise rejection. Therefore, the noise reduction for the same readout time is between $\sqrt{1.5}$ and $1.5\times$. However, MRCDS cannot remove R_{MR}, which must be accommodated by the AFE DR. Given $R_{MR}/R_{rlx} \leq 2 \times 10^5$, the AFE DR requirement is 106 dB. Although 20 dB higher than MCDS that rejects $10\times$ baseline, MRCDS still relaxes the DR requirement by 34 dB compared to when no CDS is applied. Temperature-dependent R_{MR} also limits the temperature drift rejection for MRCDS [16], [32]. The comparison between MCDS and MRCDS is summarized in Table II.

B. System Architecture

Fig. 4 shows a block diagram of the proposed sensor AFE. It consists of a sensor bias block, a CCIA, and a Zoom ADC. A low noise dc bias current, I_{in}, flows into the selected sensor, R_S, which is magnetically biased by an external Helmholtz coil. The resulting voltage, V_{in}, is amplified by the CCIA, which contains a dc reference input, V_R, and a dc servo loop (DSL) to continuously cancel the R_0 baseline. A ripple rejection loop (RRL) rejects the chopping ripple on V_{out}, which is quantized by the ADC. The Zoom ADC consists of a 6-bit SAR and a 13-bit $\Delta\Sigma$ modulator (DSM) for coarse and fine quantization, respectively. It is configured to measure V_{out} twice, either at Steps 3 and 5 for MCDS or Steps 4 and 5 for MRCDS.

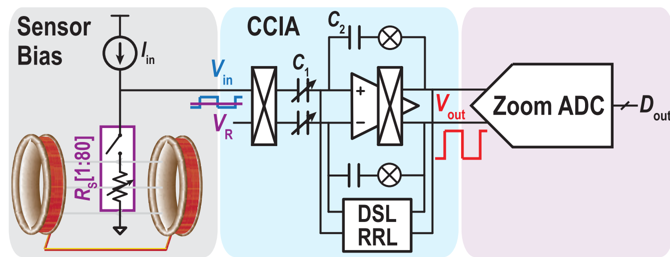

Fig. 4. Block diagram of the proposed AFE.

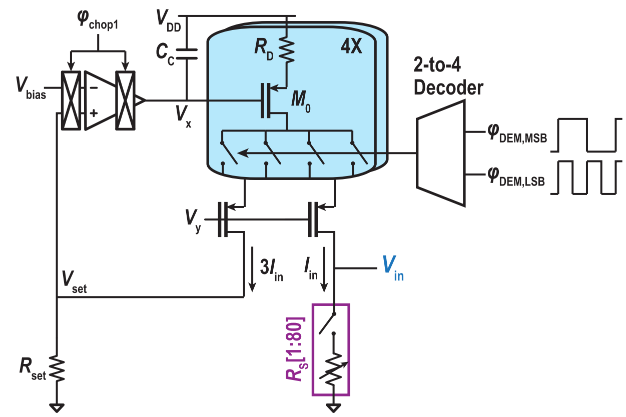

Fig. 5. Schematic of the sensor bias block with DEM.

III. CIRCUIT IMPLEMENTATION

A. Sensor Bias

Fig. 5 shows a schematic of the sensor bias block. The chopped OTA and the source degenerated current source transistors, M_0, form a negative feedback loop to provide a voltage-controlled current, $3I_{in} = V_{bias}/R_{set}$, where R_{set} is an off-chip precision resistor and V_{bias} is an externally provided dc voltage. The current is attenuated by $3\times$ to bias the selected sensor, R_S. A moscap, C_C, is used for compensation and source degeneration resistors, R_D, are used for noise reduction. The noise power at V_{in} can be written as

$$v_{n,in}^2 = R_S^2\left[\left(\frac{v_{n,op}}{3R_{set}}\right)^2 + \frac{4k_BT}{9R_{set}} + \frac{4k_BT\gamma}{g_{m0}R_DR_S} + \frac{4k_BT}{R_D} + \frac{4k_BT}{R_S}\right] \quad (2)$$

where $v_{n,op}$ is the input-referred noise of the OTA and g_{m0} is the transconductance of M_0. Since $V_{bias}/R_{set} = 3V_{in}/R_S$, larger V_{bias} and R_{set} reduce the noise contributed by the OTA and R_{set}. Having $R_D > R_S$ helps reduce the noise from M_0 and R_D. R_S is fixed from the sensor and V_{in} is limited by the sensor breakdown voltage, thus both R_{set} and R_D should be maximized for low noise but are limited by the maximum V_{bias} and minimum V_x, respectively.

To reduce the remaining $1/f$ noise from M_0, DEM is added at the cascode node. A 2-to-4 decoder directs one of the branches to the output path and the remaining three branches to the feedback path. It is configured to rotate the four

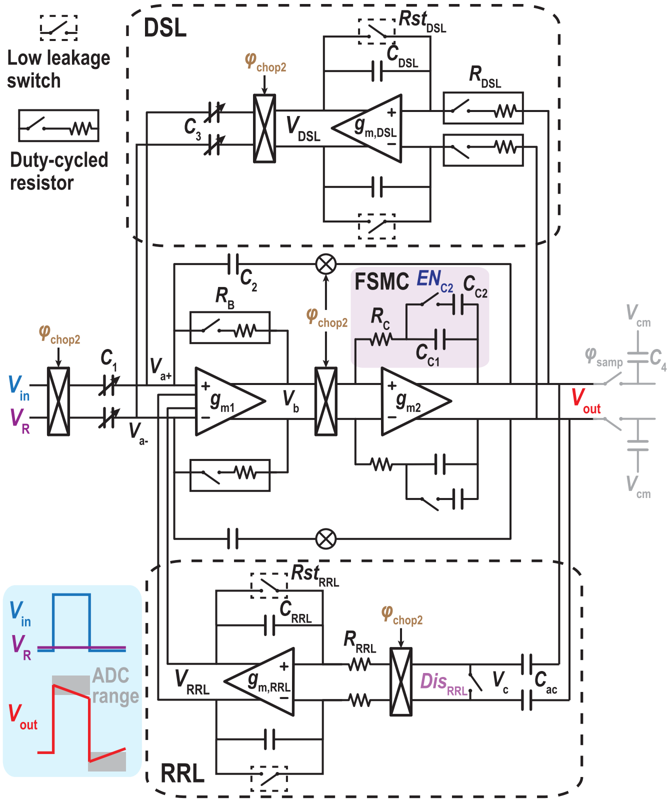

Fig. 6. Schematic of the CCIA.

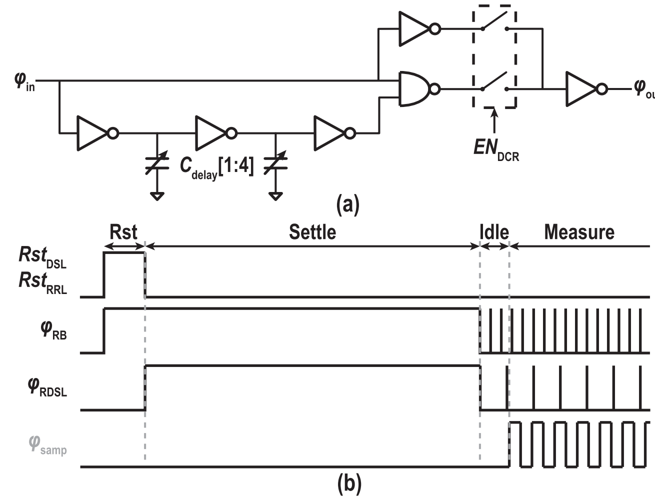

Fig. 7. (a) Schematic of the pulse generator. (b) DCR timing diagram.

branches so the $1/f$ noise from M_0 is upmodulated to the DEM frequency, f_{DEM}. The mismatch from M_0 causes ripple on V_{in} at f_{DEM} but is out-of-band and subsequently filtered by the ADC decimation filter.

B. Chopped Capacitively Coupled Instrumentation Amplifier

Fig. 6 shows a schematic of the chopped CCIA that includes a DSL and an RRL. The CCIA has a dc gain of C_1/C_2, where C_1 is a 2-bit programmable capacitor for variable gain. The reset switches used in the integrators of the DSL and RRL are implemented by low-leakage switches (leakage $<$ 1 fA in simulation) [33]. The OTA has two stages, where g_{m1} is a differential-difference folded-cascode OTA for low noise and g_{m2} is a current mirror OTA for high output swing. g_{m1} and g_{m2} are simulated to be 4.1 and 0.8 mS, respectively. Although current reuse OTAs or stacked OTAs have been reported for better efficiency, their limited swing limits the performance in this application [34]–[36]. Both OTAs use switched-capacitor common-mode feedback for high output swing. Feedback resistors, R_{B}, are implemented by duty-cycled resistors (DCRs) and an FSMC technique is proposed to maintain the stability, as will be discussed later.

The voltage across the sensor, V_{in}, and an externally provided dc voltage, V_{R}, are fed into the CCIA to form a pseudo-differential input. V_{R} is chosen to be $\sim I_{\mathrm{in}} R_0$ to reject the R_0 baseline. This can be implemented by a low-matching replica as the offset between V_{R} and V_{in} can be further nulled up to $(C_3/C_1)V_{\mathrm{DD}}$ by the DSL, which consists of an integrator and a 1-bit programmable capacitor, C_3. The input-referred noise from the DSL is $(C_3/C_1)v_{n,\mathrm{DSL}}$, where $v_{n,\mathrm{DSL}}$ is the noise of the DSL. This presents a tradeoff between the maximum tolerable offset and the noise. The OTA, $g_{\mathrm{m,DSL}}$, cannot be chopped due to the need for high input impedance and thus the $1/f$ noise from this OTA dominates the CCIA noise at low frequencies. The proposed MRCDS rejects this $1/f$ noise, thus it was not worth the effort to implement a mixed-mode DSL that would solve this [37]. Both the sensor mismatch and temperature dependence set the maximum input offset, thus the ratio of C_3/C_1. The sensor mismatch can be up to $\pm 5\%$ [38], which results in up to 25 mV of offset. Thus, C_3/C_1 must be >0.014. Since C_1 is programmable for closed-loop gain control, C_3 is tuned in tandem to maintain the ratio. To have headroom to accommodate the R_0 temperature dependence, we designed C_3/C_1 to be 0.02–0.033 in all gain configurations.

The DSL sets the CCIA high-pass corner frequency to

$$f_{\mathrm{HP}} = \frac{C_1}{C_3} \frac{1}{2\pi R_{\mathrm{DSL}} C_{\mathrm{DSL}}} \tag{3}$$

where R_{DSL} and C_{DSL} are the resistor and capacitor in the DSL integrator. Since V_{in} is a pulsed waveform, the CCIA distorts the signal and f_{HP} determines the voltage drop on V_{out} at Steps 4 and 5 (Fig. 6, bottom left). The Zoom ADC is first configured as an SAR to coarsely quantize V_{out} and then "zoom" into ± 1 $\mathrm{SAR}_{\mathrm{LSB}}$ for fine quantization, thus the voltage drop in one ADC conversion cannot exceed one $\mathrm{SAR}_{\mathrm{LSB}}$. Simulation shows that f_{HP} must be $<$1 Hz to not saturate the ADC. Given $C_3/C_1 = 0.02$–0.033, $C_{\mathrm{DSL}} = 100$ pF (limited by area), R_{DSL} must be $>$80 GΩ. Therefore, R_{DSL} is implemented by a DCR with a 32-MΩ poly-resistor and a duty cycle of $<$1/2500. Further reducing the duty cycle to save the area results in a lower switching frequency for R_{DSL}, which causes aliasing [39].

To achieve such a small duty cycle, an on-chip pulse generator was designed, as shown in Fig. 7(a), where 2-bit programmable capacitors, C_{delay}, adjust the pulsewidth to compensate for process variation [34]. The pulsewidth was simulated to be

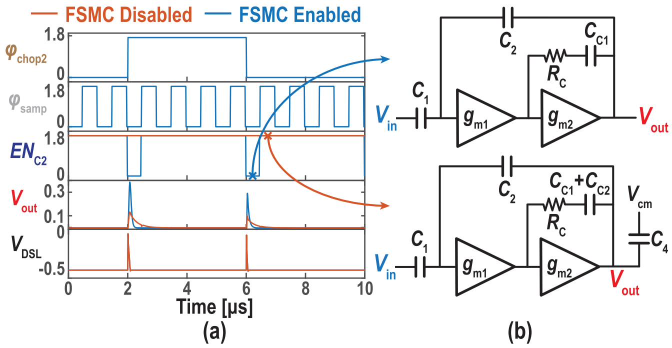

Fig. 8. (a) FSMC timing diagram and simulated transient results. (b) Equivalent schematics.

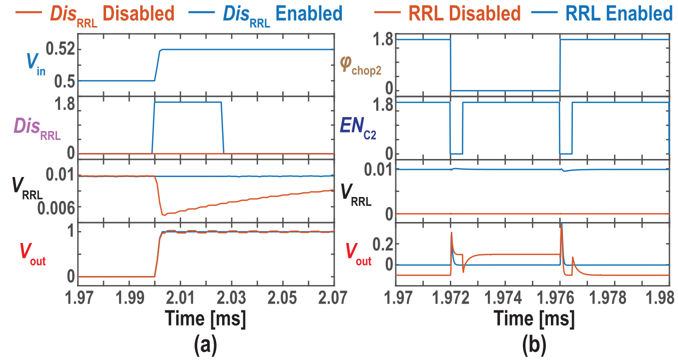

Fig. 9. RRL timing diagram and simulated results during (a) MRX and (b) FSMC.

1.3–3.8 ns, based on C_{delay}. Since the multiplexed sensor array is read in a time-sequenced manner, the settling time when switching between sensors significantly increases the array readout time. Thus, fast-settling DCRs are used to improve the settling [17]. In Fig. 7(b), the DSL and RRL are first reset when switching sensors. The switches for R_{B} are kept closed to generate a low impedance path from V_{b} to $V_{\text{a}+/-}$, enabling fast settling at $V_{\text{a}+/-}$. When the DSL starts to operate, the switches for R_{DSL} are closed so the DSL integrator can quickly find the input offset due to the low impedance. In both the reset and settling phases, $EN_{\text{DCR}} = 0$ so $\varphi_{\text{out}} = \varphi_{\text{in}}$ for both DCRs. After the CCIA is fully settled, EN_{DCR} changes to 1 to place both DCRs into duty-cycled mode. Following a short idle period, the ADC sampling clock, φ_{samp}, starts quantizing V_{out}.

To ensure the CCIA stability, Miller compensation is commonly used to create a dominant pole internally with the nondominant pole at the output due to the ADC sampling capacitor, C_4. Unfortunately, dc offsets from the input and V_{DSL} cause signal-dependent charge injection, which require sufficient settling time to maintain the linearity. The settling time is inversely proportional to the CCIA bandwidth ($g_{\text{m1}}/C_{\text{C}}$). To ensure proper settling before ADC sampling, the most straightforward solution is to increase g_{m1}, resulting in an increased power consumption.

We propose an alternative approach, FSMC, whereby the compensation is dynamically changed, as shown in Fig. 8(a). A similar technique was used in an LDO to compensate different loads [40], but is different in that FSMC changes the compensation periodically. The timing of the CCIA and ADC is adjusted so that the sample switch is turned off right before every chopping edge to ensure that C_4 does not load V_{out} when the spikes appear. EN_{C2} disconnects C_{C2} so that only C_{C1} compensates the CCIA, enabling fast spike settling (due to the higher bandwidth). EN_{C2} closes the switches right before the next rising edge of φ_{samp} to guarantee C_{C2} is included to compensate the CCIA when C_4 loads V_{out}. The equivalent schematics in both phases of operation are illustrated in Fig. 8(b). Simulation results show that although FSMC results in larger spikes due to the higher bandwidth, the spikes settle much faster than the case that always connects $C_{\text{C1}} + C_{\text{C2}}$. A nulling poly-resistor, R_C, is placed in series with the compensation capacitors to generate a zero that cancels the nondominant pole. The value of R_C can be calculated as

$$R_{\text{C}} = \frac{C_{\text{C1}} + C_2}{g_{\text{m2}} C_{\text{C1}}} \tag{4}$$

$$R_{\text{C}} = \frac{C_{\text{C1}} + C_{\text{C2}} + C_4}{g_{\text{m2}}(C_{\text{C1}} + C_{\text{C2}})} \tag{5}$$

for $EN_{\text{C2}} = 0$ and $EN_{\text{C2}} = 1$, respectively. By selecting the capacitances properly, R_{C} can be equal in both cases. Inaccurate R_{C} causes mismatch between the pole and zero, but would not increase the settling time since the pole-zero doublet is placed close to the unity-gain bandwidth [41]. C_{C2} is designed to be 3× larger than C_{C1} to have a worst case phase margin of >75°. The proposed FSMC technique relaxes g_{m1} by 4× and thus reduces the CCIA power consumption by 2.5×.

An RRL eliminates the ripple from the OTA g_{m1} offset [42]. The ripple at f_{chop2} passes through ac-coupling capacitors, C_{ac}, and is then downmodulated to dc. After the integrator, the RRL dynamically adjusts the g_{m1} offset through another differential pair, that consumes 10× less power than the main differential pair in the OTA. Compared to a conventional RRL, one more switch is added after C_{ac} to disable the RRL during the voltage pulses on V_{out}. Without this switch, the instantaneous voltage changes at V_{out} pass through C_{ac} to change V_{RRL}, thus creating an additional ripple, as illustrated in Fig. 9(a). It is simulated to take >100 μs to settle, significantly increasing the deadzone time. Instead, the switch is turned on ($Dis_{\text{RRL}} = 1$) right before the voltage changes to short the integrator inputs, thus V_{RRL} remains unchanged. After V_{out} is settled, the switch is turned off ($Dis_{\text{RRL}} = 0$) so the RRL returns to normal operation and keeps track of the g_{m1} offset. It should be mentioned that the RRL is required for FSMC, as shown in Fig. 9(b). Without the RRL, the ripple leads to a different V_{out} before and after $EN_{\text{C2}} = 0$. When EN_{C2} changes from 0 to 1, g_{m1} needs to charge C_{C2}, leading to another settling issue. The RRL cancels the V_{out} ripple so the voltage remains unchanged before and after $EN_{\text{C2}} = 0$. Accordingly, g_{m1} only needs to settle the charge injection from the EN_{C2} switches, which include half-sized dummy switches to absorb the charge injection [43].

C. Analog-to-Digital Converter

A Zoom ADC is a hybrid ADC for dc-input, high-resolution conversion [44]. Fig. 10(a) shows the block diagram, where a

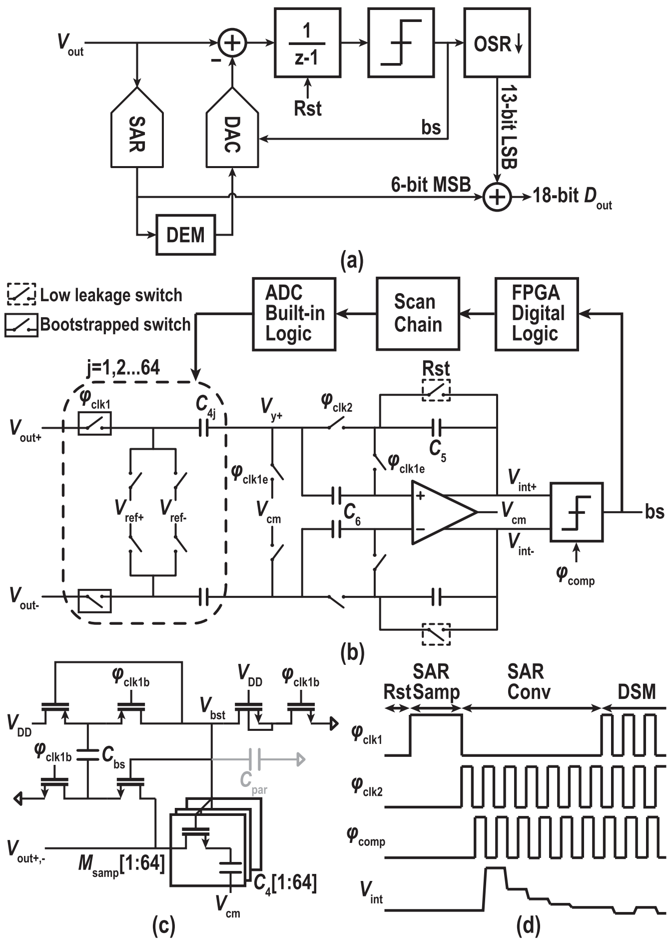

Fig. 10. (a) Block diagram and (b) schematic of the Zoom ADC, (c) bootstrapped sampling switch, and (d) ADC timing diagram.

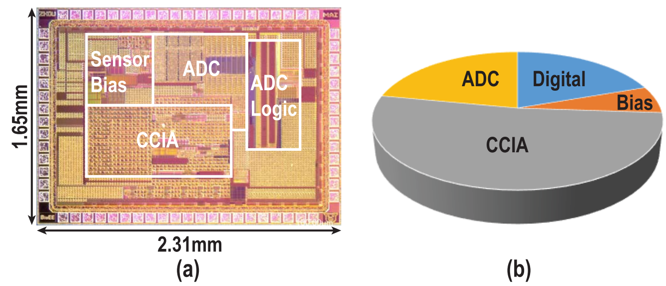

Fig. 11. (a) Annotated die photo. (b) Power distribution.

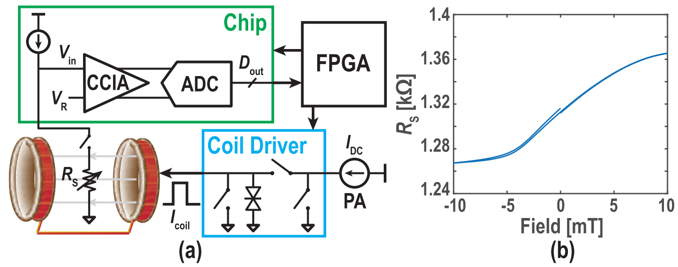

Fig. 12. (a) Measurement setup. (b) Measured sensor response to an applied field.

6-bit SAR coarsely quantizes V_{out} and then adjusts the reference voltages of the DSM with a 6-bit DAC. A pseudorandom bit sequence (PRBS) for non-segmented DEM is implemented off-chip by an FPGA to shape the DAC mismatch [45]. The mismatch-shaping DEM turns the spurious tones into white noise, which is spectrally shaped [46]. A first-order, single-bit DSM quantizes the residue voltage with an oversampling ratio (OSR) of 9956 and an on-chip counter decimates the bitstream, providing a 13-bit output. Since the SAR result needs to be extended by ± 1 SAR_{LSB} to avoid saturating the DSM, the Zoom ADC has a resolution of 18-bit. The sampling frequency is 1 MHz for a bandwidth of 100 Hz. The voltage residue during the DSM phase cannot exceed ± 1 SAR_{LSB}, so the maximum input frequency, f_{sig}, is

$$f_{sig} < \frac{V_{ref}}{2\pi A_{sig} T_{ADC} 2^6} \tag{6}$$

where $V_{ref} = V_{ref+} - V_{ref-}$ is the ADC reference voltage, A_{sig} is the input signal amplitude, and T_{ADC} is the ADC cycle time. Considering a full-scale sinusoidal input ($A_{sig} = V_{ref}/2$), $T_{ADC} = T_{cycle} = 10$ ms, f_{sig} must be <0.5 Hz to not saturate the ADC.

The implementation of the Zoom ADC is shown in Fig. 10(b). It consists of a switched-capacitor integrator, a dynamic latched comparator, and digital logic that generates the clocks. 64× 100 fF unit-caps implement the 6-bit, non-segmented CDAC. Bootstrapped sampling switches improve the linearity from 10.7 to 17.7 bits in simulation, as shown in Fig. 10(c). Instead of using 64 independent switches, the switches share the control transistors and the level shift capacitor, C_{bs}. This reduces the area and minimizes the parasitic capacitance, C_{par}, at V_{bst}, which attenuates V_{GS} of M_{samp} during the sampling phase. The ADC timing diagram is shown in Fig. 10(d). The ADC is first configured as an SAR that samples V_{out} with 3× periods for settling. Then, 6× SAR conversion cycles are conducted with charge redistribution between C_4 and C_5. Afterward, the SAR output adjusts the reference voltages for the DSM. Specifically, $SAR_{out} \pm 1$ unit-caps C_{4j} connect to V_{ref+}, while the others connect to V_{ref-}, where D_{out} determines the sign. Timing of the Zoom ADC is critical for proper operation. The comparator clock, φ_{comp}, needs to be set up such that there is enough time for the delays of the comparator, DEM propagation, and scan chain. These delays limit the ADC speed. The reference voltages of the ADC, V_{ref+} and V_{ref-}, are set to V_{DD} and GND, respectively. Like a conventional DSM, bottom plate sampling and correlated double sampling are applied for high linearity and low $1/f$ noise, respectively.

IV. Measurement Results

This chip was fabricated in a 180-nm CMOS process. An annotated die photo is shown in Fig. 11(a). It operates from a single 1.8-V supply and consumes 4.32 mW excluding the sensor bias, which is dependent on the sensor resistance and consumes 3.9 mW for the 1.3-kΩ sensors used in this work. The relative power contributions of each block (CCIA: 52%, ADC: 22%, digital: 20%, bias: 6%) are plotted in Fig. 11(b).

The measurement setup is shown in Fig. 12(a). A power amplifier (Kepco BOP 36-12ML) is connected to a custom coil driver and a Helmholtz coil, which generates a 3-mT

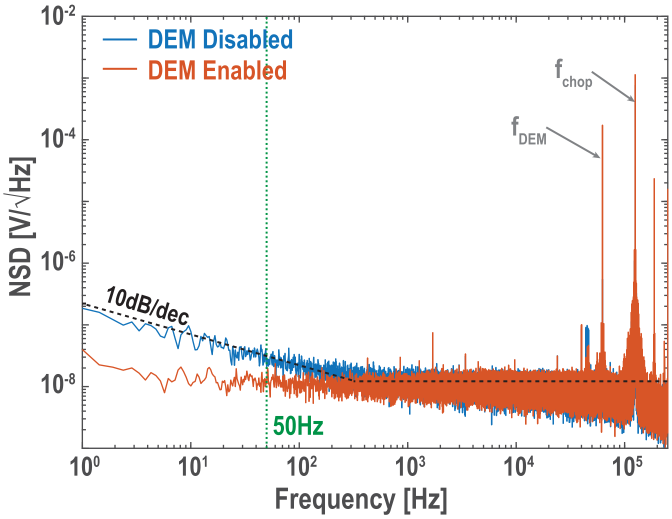

Fig. 13. Measured sensor bias noise spectra.

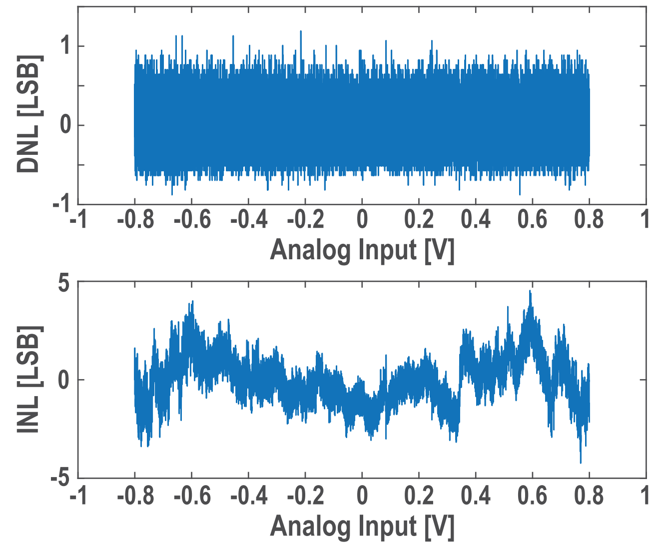

Fig. 15. Measured ADC DNL and INL.

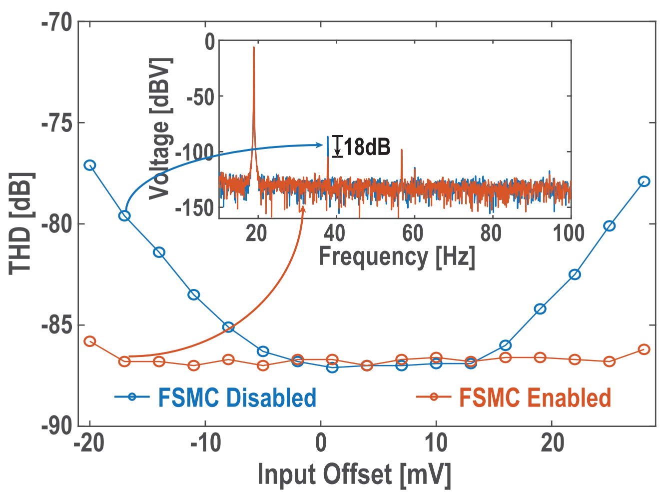

Fig. 14. Measured CCIA linearity versus input offset.

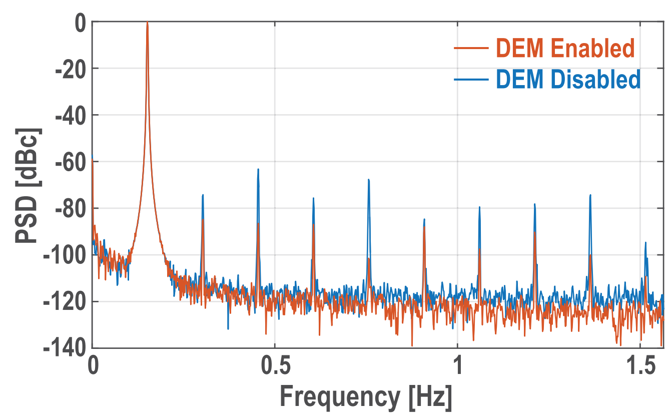

Fig. 16. Measured spectra of the signal path (CCIA+ADC).

pulsed magnetic field for 10 ms. The coil driver, which is controlled by the FPGA (Opal Kelly XEM6310), enables a fast decay magnetic field for the sensor to minimize the deadzone (<2 μs) [29]. The same FPGA is used for clocking and control signals for the chip, as well as capturing data from the ADC. The sensor array (MagArray, Inc.) is composed of an 8×10 array of sensors, where each sensor is 100×100 μm^2. The array is read out in a time-sequenced manner where one sensor is selected at a time by two off-chip analog muxes. The sensors have an average R_0 of 1.3 kΩ and an average transduction coefficient of 9 Ω/mT, as shown in Fig. 12(b). The MR ratio, defined as $(R_{max} - R_{min})/R_{min}$, is 7.74% and the sensor mismatch within the same die is 1.6% (1σ).

Fig. 13 shows the measured noise spectra at node V_{in} in the sensor bias block. The DEM reduces the $1/f$ noise corner frequency from $\sim$300 Hz to $<$10 Hz and the spot noise at 50 Hz by 2.2$\times$ to 13.6 nV/$\sqrt{}$Hz. It should be noted that only the spot noise at 50 Hz is relevant because MRCDS eliminates $1/f$ noise that is $<$50 Hz for $T_{cycle} = 10$ ms. Upmodulated $1/f$ noise and current mirror mismatch generate tones at f_{DEM} and f_{chop}, which are out-of-band and filtered by the ADC decimation filter.

Fig. 14 shows the measured CCIA total harmonic distortion (THD) versus the input dc offset using a sinusoidal input with an output swing of 1.6 V_{pp} superimposed on the dc offset. This range covers up to a 4.3-mT magnetic field. Larger offset leads to more distortion due to incomplete settling of the ADC from the DSL. The FSMC technique settles these spikes faster and improves the CCIA linearity variation from 10 to 1.2 dB across the input offset range. The spectra at V_{os} = -17 mV have an 18-dB improvement in HD2. The asymmetric input offset range is due to the DSL offset. The linearity across the input range is $>$85 dB. The measured input-referred spot noise at 50 Hz is 6.6 nV/$\sqrt{}$Hz.

The ADC was characterized using a dc sweep histogram by an audio analyzer (APx555B). Fig. 15 shows the measured differential nonlinearity (DNL) and integral nonlinearity (INL) over the input range of -0.8–0.8 V. The ADC has a DNL of -0.87/+1.19 LSB and an INL of -4.2/+4.5 LSB. The equivalent 95-dB SFDR is 10 dB higher than the CCIA THD. The ADC noise PSD is 745 nV/$\sqrt{}$Hz, which is 14.9 nV/$\sqrt{}$Hz when input-referred to the CCIA input. This is comparable to the noise from the other two stages, thus 18-bit resolution is

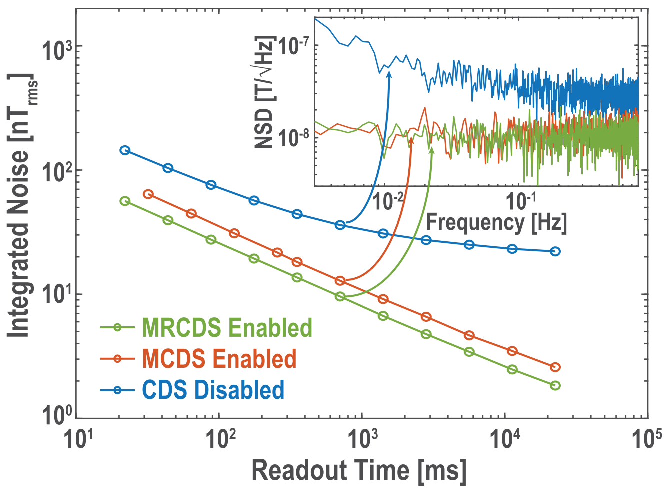

Fig. 17. Measured integrated noise versus readout time.

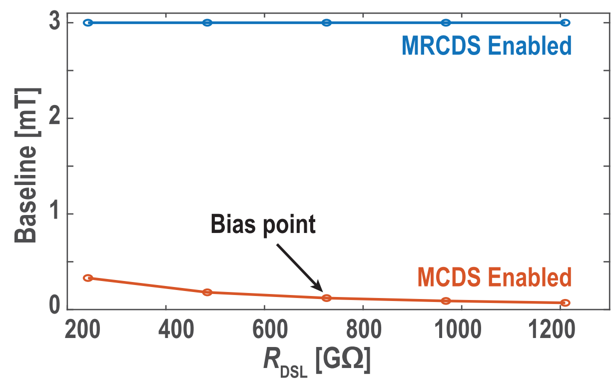

Fig. 18. Measured input-referred baseline versus DSL integrator resistance.

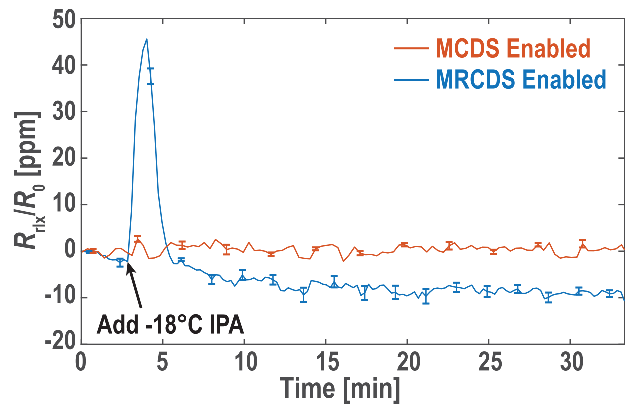

Fig. 19. Measured temperature dependence.

required to reduce the quantization noise. Although the CCIA gain can be increased to reduce the ADC noise contribution, it is in contrast with the DR requirement in MRCDS.

The signal path (CCIA+ADC) was characterized by applying a fully-differential sinusoid to the CCIA. The input frequency is 0.154 Hz, which satisfies (6) to not saturate the ADC. Fig. 16 shows the measured spectra, with and without DEM enabled. The spectra are truncated for a readout time of 704 ms. The SNDR improved from 61 to 81 dB by enabling the DEM. It should be noted that the $1/f$ noise shown in the spectra can be eliminated when MCDS or MRCDS is applied.

Fig. 17 shows the measured input-referred integrated noise versus the readout time. The proposed MRCDS has a 22-ms readout time, which consists of 2 ms for reset and 20 ms for measurement. MCDS needs 32 ms due to the additional cycle. The data can be averaged to lower the noise with a longer readout time. Both MCDS and MRCDS show a linear tradeoff between the readout time and the integrated noise on a log scale because the $1/f$ noise is eliminated. Without CDS, the residual $1/f$ noise limits the resolution for long readout times. MRCDS was measured to reduce the integrated noise by 1.34× compared to MCDS, which matches the theoretical range of $\sqrt{1.5}$–1.5×.

The input-referred baseline was measured for both MCDS and MRCDS, as shown in Fig. 18. MRCDS does not reject the R_{MR} baseline, and thus has higher baseline than MCDS. The residual baseline in MCDS comes from the DSL. Although f_{HP} in the CCIA is low enough to not saturate the ADC, it still distorts the waveform, leading to a residual baseline. Increasing R_{DSL} decreases f_{HP}, and thus reduces the baseline. The AFE has a measured baseline of 0.12 mT in the standard configuration of the CCIA, that is 25× smaller than MRCDS.

Fig. 19 shows the measured temperature response. Cold isopropyl alcohol (−18 °C) was added on the sensor surface at $t = 3$ min while the system was continuously measuring for 33 min. MR sensors typically have temperature coefficients (TCs) of 10.4 ppm/°C [17]. MRCDS and MCDS reduce the temperature dependence to 1.24 and 0.07 ppm/°C, respectively. Although both R_0 and R_{MR} are temperature sensitive, R_0 drift is rejected by both the DSL and the CDS techniques. R_{MR} drift, however, can only be rejected by MCDS because MRCDS still contains the R_{MR} baseline. The AFE was measured to have a smaller temperature dependence (0.06 ppm/°C) and thus would not limit the performance.

Biological experiments were conducted for proof-of-principle demonstration. 40-nm MNPs (Ocean Nano-Technologies SHS-30-01) were dried on the sensor surface to mimic the MIA described in Fig. 1. To observe the temporal relaxation signal, an off-chip ADC (NI-6289) measured the CCIA output with a sampling rate of 500 kS/s and an 18-bit resolution. It should be mentioned that the on-chip Zoom ADC does not have the speed to capture this temporal signal but will be used to integrate the signal for higher efficiency in MIA experiments. Fig. 20(a) shows the measured relaxation curves of 70 sensors. With a relaxation time of 10 ms, the signal amplitude ranges from 1200 to 1500 ppm, depending on the surface coverage of the MNPs. Normalizing the relaxation curves by their final amplitudes, all curves follow (1), with a t_C of 19.3 ms. While t_C is highly dependent on the magnetization time and the magnetic field strength, the measured t_C matches empirical results in the literature [27].

An MIA was then conducted to demonstrate the system, as shown in Fig. 20(b). The first row of the sensor array (ten sensors) was covered by epoxy to prevent MNP binding, thus serving as a negative control. The other 70 sensors were functionalized with NHS-Biotin through APTES surface chemistry. Briefly, the sensors were immersed in 100 μL of 1% KOH in deionized water (DIW) for 10 min at 37 °C.

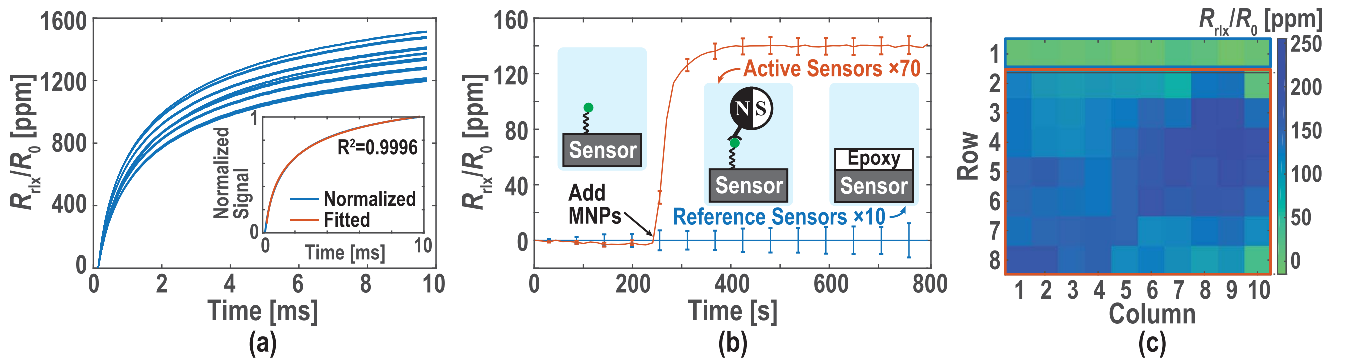

Fig. 20. (a) Measured temporal relaxation curve for dried MNPs. (b) MIA real-time binding curves for active and reference sensors. (c) MIA coverage map.

TABLE III

COMPARISON WITH STATE-OF-THE-ART MAGNETIC SENSOR AFES

	H. Wang ISSCC'09 [11]	D.A. Hall JSSC'13 [16]	T. Costa TBCAS'17 [15]	X. Zhou TBCAS'19 [17]	P. Liu JSSC'12 [12]	S. Gambini JSSC'13 [13]	**This work (MCDS)**	**This work (MRCDS)**
Sensor Type	*LC*	GMR	GMR	GMR	Hall	Hall	**GMR**	
Sensor Resistance (kΩ)	N/A	1.92	0.85	0.15	N/A	N/A	**1.3**	
MR Ratio (%)	N/A	9.2	5.37	9.04	N/A	N/A	**7.74**	
MNP Size (nm)	1,000	50	250	50	1,000	1,000	**40**	
Technology Node (μm)	0.13	0.18	0.35	0.18	0.18	0.18	**0.18**	
Sensing Method	Magneto	Magneto	Magneto	Magneto	MRX	MRX	**MRX**	
AFE Architecture	*LC* oscillator	TIA	Amplifier	PGA + Mixer	PGA	V/I Converter	**CCIA**	
ADC Architecture	VCO-based	ΔΣ	No ADC	Inc. ΔΣ	No ADC	Inc. ΔΣ	**Zoom**	
Input-referred Integrated Noise (nT$_{rms}$)	N/A	32.8$^{\psi}$ 49	11.5$^{\psi}$ N/A	436$^{\psi}$ 460	15$^{\psi}$ N/A	N/A$^{\psi}$ 1207	**9.6$^{\psi}$ 13**	**6.9$^{\psi}$ 9.7**
Readout Time/Ch. (ms)	400	250	1,000	11	64,000	50	**704**	
Power/Ch. (mW)*	N/A	2.24$^{\psi}$ 3.15	4.9$^{\psi}$	0.43$^{\psi}$ 1.39	6.2$^{\psi}$	N/A$^{\psi}$ 0.825	**2.5$^{\psi}$ 4.32**	
Area/Ch. (mm^2)	N/A	0.219	3.17	0.249	N/A	0.012	**1.92**	
Number of Ch.	8	16	1	1	1	160	**1**	
Input-referred Baseline (mT)	N/A	7.09	1.84	<0.235	<0.001	0.007	**0.12**	**3**
Temperature Correction	Yes	Yes	No	Yes	Yes	Yes	**Yes**	**No**
Resolution FoM† (nT^2·mJ)	N/A	602$^{\psi}$ 1,891	648$^{\psi}$ N/A	899$^{\psi}$ 3,235	89,280$^{\psi}$ N/A	N/A$^{\psi}$ 60,143	**162$^{\psi}$ 514**	**84$^{\psi}$ 286**

* Power/Ch does not include sensor bias and magnetic field generator. $^{\psi}$ Does not include ADC. † FoM=Resolution^2×Energy/Conversion.

The sensors were then washed with 300 μL of DIW and allowed to dry. 70 μL of 100% APTES was added for 1 h at 37 °C (paraffin was wrapped around the sensor well to prevent evaporation). The sensors were then washed 5× with 300 μL of phosphate-buffered saline (PBS) and 50 μL of NHS-Biotin (1 mg/mL in dimethyl sulfoxide) was added to the sensors for 1 h at 37 °C prior to washing 3× with 300 μL of PBS. Blocking was accomplished by adding 100 μL of 10% bovine serum albumin (BSA) in PBS for 15 min at 37 °C before removal and washing 3× with 300 μL of PBS. Lastly, 100 μL of PBS was added before the sensor array was moved to the measurement setup.

After removing the PBS and adding 50 μL of MNPs, the active sensors showed signals of ∼140 ppm, while the reference sensors showed no signal. The error bars represent one standard error. Since each sensor has a slightly different temperature dependence, the error bars increased with time because MRCDS was used. Fig. 20(c) illustrates the signal map of the 8 × 10 sensor array, where each signal amplitude represents the signal difference before and after adding the MNPs for each sensor. Compared to the dried MNPs, the MIA shows ∼10× smaller signal amplitude because of the increased distance between the MNPs and the sensor as well as the lower density due to the binding equilibrium. The signal variation is mainly from different number of binding sites on each sensor due to the blanket functionalization procedure used here.

This work is summarized in Table III. Compared to other magnetic sensor front-ends, this work has the lowest input-referred noise, along with comparable power consumption and readout time. It results in a best-reported FoM of 286 and 514 nT^2 · mJ, respectively, for MRCDS and MCDS, which is 6.6× better than other magnetic AFEs and 210× better than MRX-based AFEs. While MRCDS shows the best FoM, MCDS has advantages on the baseline reduction and temperature drift cancellation. This work supports both techniques.

V. Conclusion

In this article, we present an MR sensor AFE with a Zoom ADC to detect MNP relaxation. A sensor bias block with DEM reduces $1/f$ noise from the bias transistors by $2.2\times$. A CCIA with FSMC reduces the CCIA power consumption by $2.5\times$, while maintaining the linearity and stability. An 18-bit Zoom ADC quantizes the CCIA outputs with an INL of 4.5 LSB. The system uses either MRCDS or MCDS to capture the signal, reject $R0$ baseline, and remove noise/time tradeoff limitation by eliminating $1/f$ noise. While MCDS is better for baseline rejection and temperature drift cancellation, MRCDS provides better $1/f$ noise rejection and takes less readout time, thus resulting in a better FoM. Experiments with dried MNP and an MIA were conducted to demonstrate the system. This work has a best-reported FoM, that is $6.6\times$ better than other magnetic AFEs and $210\times$ better than MRX-based AFEs.

References

[1] S. Vashist, "Point-of-care diagnostics: Recent advances and trends," *Biosensors*, vol. 7, no. 4, p. 62, Dec. 2017.

[2] S. Nayak, N. R. Blumenfeld, T. Laksanasopin, and S. K. Sia, "Point-of-care diagnostics: Recent developments in a connected age," *Anal. Chem.*, vol. 89, no. 1, pp. 102–123, Dec. 2016.

[3] S. K. Vashist, P. B. Luppa, L. Y. Yeo, A. Ozcan, and J. H. T. Luong, "Emerging technologies for next-generation point-of-care testing," *Trends Biotechnol.*, vol. 33, no. 11, pp. 692–705, Nov. 2015.

[4] A. Thiha and F. Ibrahim, "A colorimetric enzyme-linked immunosorbent assay (ELISA) detection platform for a point-of-care dengue detection system on a lab-on-compact-disc," *Sensors*, vol. 15, no. 5, pp. 11431–11441, May 2015.

[5] J. D. Newman and A. P. F. Turner, "Home blood glucose biosensors: A commercial perspective," *Biosensors Bioelectron.*, vol. 20, no. 12, pp. 2435–2453, Jun. 2005.

[6] K. M. Koczula and A. Gallotta, "Lateral flow assays," *Essays Biochem.*, vol. 60, no. 1, pp. 111–120, Jun. 2016.

[7] J. S. Swensen *et al.*, "Continuous, real-time monitoring of cocaine in undiluted blood serum via a microfluidic, electrochemical aptamer-based sensor," *J. Amer. Chem. Soc.*, vol. 131, no. 12, pp. 4262–4266, Apr. 2009.

[8] H. Jiang, X. Zhou, S. Kulkarni, M. Uranian, R. Seenivasan, and D. A. Hall, "A sub-1 μW multiparameter injectable BioMote for continuous alcohol monitoring," in *Proc. IEEE Custom Integr. Circuits Conf. (CICC)*, Apr. 2018, pp. 1–4.

[9] N. Sun, T.-J. Yoon, H. Lee, W. Andress, R. Weissleder, and D. Ham, "Palm NMR and 1-chip NMR," *IEEE J. Solid-State Circuits*, vol. 46, no. 1, pp. 342–352, Jan. 2011.

[10] K.-M. Lei, H. Heidari, P.-I. Mak, M.-K. Law, F. Maloberti, and R. P. Martins, "A handheld high-sensitivity micro-NMR CMOS platform with B-field stabilization for multi-type biological/chemical assays," *IEEE J. Solid-State Circuits*, vol. 52, no. 1, pp. 284–297, Jan. 2017.

[11] H. Wang, Y. Chen, A. Hassibi, A. Scherer, and A. Hajimiri, "A frequency-shift CMOS magnetic biosensor array with single-bead sensitivity and no external magnet," in *IEEE Int. Solid-State Circuits Conf. (ISSCC) Dig. Tech. Papers*, Feb. 2009, pp. 438–439.

[12] P. P. Liu *et al.*, "Magnetic relaxation detector for microbead labels," *IEEE J. Solid-State Circuits*, vol. 47, no. 4, pp. 1056–1064, Apr. 2012.

[13] S. Gambini, K. Skucha, P. P. Liu, J. Kim, and R. Krigel, "A 10 kPixel CMOS Hall sensor array with baseline suppression and parallel readout for immunoassays," *IEEE J. Solid-State Circuits*, vol. 48, no. 1, pp. 302–317, Jan. 2013.

[14] S.-J. Han, H. Yu, B. Murmann, N. Pourmand, and S. X. Wang, "A high-density magnetoresistive biosensor array with drift-compensation mechanism," in *IEEE Int. Solid-State Circuits Conf. (ISSCC) Dig. Tech. Papers*, Feb. 2007, pp. 168–594.

[15] T. Costa, F. A. Cardoso, J. Germano, P. P. Freitas, and M. S. Piedade, "A CMOS front-end with integrated magnetoresistive sensors for biomolecular recognition detection applications," *IEEE Trans. Biomed. Circuits Syst.*, vol. 11, no. 5, pp. 988–1000, Oct. 2017.

[16] D. A. Hall, R. S. Gaster, K. A. A. Makinwa, S. X. Wang, and B. Murmann, "A 256 pixel magnetoresistive biosensor microarray in 0.18 μm CMOS," *IEEE J. Solid-State Circuits*, vol. 48, no. 5, pp. 1290–1301, May 2013.

[17] X. Zhou, M. Sveiven, and D. A. Hall, "A CMOS magnetoresistive sensor front-end with mismatch-tolerance and sub-ppm sensitivity for magnetic immunoassays," *IEEE Trans. Biomed. Circuits Syst.*, vol. 13, no. 6, pp. 1254–1263, Dec. 2019.

[18] R. S. Gaster *et al.*, "Matrix-insensitive protein assays push the limits of biosensors in medicine," *Nature Med.*, vol. 15, no. 11, pp. 1327–1332, Nov. 2009.

[19] X. Zhou, C.-C. Huang, and D. A. Hall, "Magnetoresistive biosensors for quantitative proteomics," *Proc. SPIE*, vol. 10352, Aug. 2017, Art. no. 103520F.

[20] M.-D. Cubells-Beltrán *et al.*, "Integration of GMR sensors with different technologies," *Sensors*, vol. 16, no. 6, p. 939, Jun. 2016.

[21] S.-J. Han *et al.*, "CMOS integrated DNA microarray based on GMR sensors," in *IEDM Tech. Dig.*, Dec. 2006, pp. 1–4.

[22] P. P. Freitas, R. Ferreira, S. Cardoso, and F. Cardoso, "Magnetoresistive sensors," *J. Phys. Condens. Matter*, vol. 19, no. 16, Apr. 2007, Art. no. 165221.

[23] W. F. Brown, "Thermal fluctuations of a single-domain particle," *Phys. Rev.*, vol. 130, no. 5, pp. 1677–1686, Jun. 1963.

[24] L. Néel, "Théorie du traînage magnétique des substances massives dans le domaine de Rayleigh," *J. Phys. Radium*, vol. 11, no. 2, pp. 49–61, 1950.

[25] F. Ludwig, E. Heim, and M. Schilling, "Magnetorelaxometry of magnetic nanoparticles—A new method for the quantitative and specific analysis of biomolecules," in *Proc. 4th IEEE Conf. Nanotechnol.*, Aug. 2004, pp. 245–248.

[26] R. W. Chantrell, S. R. Hoon, and B. K. Tanner, "Time-dependent magnetization in fine-particle ferromagnetic systems," *J. Magn. Magn. Mater.*, vol. 38, no. 2, pp. 133–141, Sep. 1983.

[27] C.-C. Huang, X. Zhou, and D. A. Hall, "Giant magnetoresistive biosensors for time-domain magnetorelaxometry: A theoretical investigation and progress toward an immunoassay," *Sci. Rep.*, vol. 7, no. 1, pp. 1–10, Apr. 2017.

[28] R. Kötitz, W. Weitschies, L. Trahms, and W. Semmler, "Investigation of brownian and Néel relaxation in magnetic fluids," *J. Magn. Magn. Mater.*, vol. 201, nos. 1–3, pp. 102–104, Jul. 1999.

[29] X. Zhou, C.-C. Huang, and D. A. Hall, "Giant magnetoresistive biosensor array for detecting magnetorelaxation," *IEEE Trans. Biomed. Circuits Syst.*, vol. 11, no. 4, pp. 755–764, Aug. 2017.

[30] K. A. A. Makinwa, "Smart temperature sensors in standard CMOS," *Procedia Eng.*, vol. 5, pp. 930–939, Jan. 2010.

[31] H. Jiang, C.-C. Huang, M. R. Chan, and D. A. Hall, "A 2-in-1 temperature and humidity sensor with a single FLL wheatstone-bridge front-end," *IEEE J. Solid-State Circuits*, vol. 55, no. 8, pp. 2174–2185, Aug. 2020.

[32] K.-M.-H. Lenssen, A. E. T. Kuiper, J. J. van den Broek, R. A. F. van der Rijt, and A. van Loon, "Sensor properties of a robust giant magnetoresistance material system at elevated temperatures," *J. Appl. Phys.*, vol. 87, no. 9, pp. 6665–6667, May 2000.

[33] M. O'Halloran and R. Sarpeshkar, "A 10-nW 12-bit accurate analog storage cell with 10-aA leakage," *IEEE J. Solid-State Circuits*, vol. 39, no. 11, pp. 1985–1996, Nov. 2004.

[34] H. Chandrakumar and D. Markovic, "A high dynamic-range neural recording chopper amplifier for simultaneous neural recording and stimulation," *IEEE J. Solid-State Circuits*, vol. 52, no. 3, pp. 645–656, Mar. 2017.

[35] S. Mondal and D. A. Hall, "A 13.9-nA ECG amplifier achieving 0.86/0.99 NEF/PEF using AC-coupled OTA-stacking," *IEEE J. Solid-State Circuits*, vol. 55, no. 2, pp. 414–425, Feb. 2020.

[36] L. Shen, N. Lu, and N. Sun, "A 1V 0.25 μW inverter-stacking amplifier with 1.07 noise efficiency factor," in *Proc. Symp. VLSI Circuits*, Jun. 2017, pp. C140–C141.

[37] U. Ha, J. Lee, M. Kim, T. Roh, S. Choi, and H.-J. Yoo, "An EEG-NIRS multimodal SoC for accurate anesthesia depth monitoring," *IEEE J. Solid-State Circuits*, vol. 53, no. 6, pp. 1830–1843, Jun. 2018.

[38] C. Reig, D. Ramırez, F. Silva, J. Bernardo, and P. Freitas, "Design, fabrication, and analysis of a spin-valve based current sensor," *Sens. Actuators A, Phys.*, vol. 115, nos. 2–3, pp. 259–266, Sep. 2004.

[39] H. Chandrakumar and D. Marković, "An 80-mVpp linear-input range, 1.6-GΩ input impedance, low-power chopper amplifier for closed-loop neural recording that is tolerant to 650-mVpp common-mode interference," *IEEE J. Solid-State Circuits*, vol. 52, no. 11, pp. 2811–2828, Nov. 2017.

[40] C. Zhan, G. Cai, and W.-H. Ki, "A transient-enhanced output-capacitor-free low-dropout regulator with dynamic Miller compensation," *IEEE Trans. Very Large Scale Integr. (VLSI) Syst.*, vol. 27, no. 1, pp. 243–247, Jan. 2019.

[41] B. Y. T. Kamath, R. G. Meyer, and P. R. Gray, "Relationship between frequency response and settling time of operational amplifiers," *IEEE J. Solid-State Circuits*, vol. SSC-9, no. 6, pp. 347–352, Dec. 1974.

[42] Q. Fan, F. Sebastiano, J. H. Huijsing, and K. A. A. Makinwa, "A 1.8 μW 60 nV/$\sqrt{\text{Hz}}$ capacitively-coupled chopper instrumentation amplifier in 65 nm CMOS for wireless sensor nodes," *IEEE J. Solid-State Circuits*, vol. 46, no. 7, pp. 1534–1543, Jul. 2011.

[43] C. C. Enz and G. C. Temes, "Circuit techniques for reducing the effects of op-amp imperfections: Autozeroing, correlated double sampling, and chopper stabilization," *Proc. IEEE*, vol. 84, no. 11, pp. 1584–1614, Nov. 1996.

[44] Y. Chae, K. Souri, and K. A. A. Makinwa, "A 6.3 μW 20 bit incremental zoom-ADC with 6 ppm INL and 1 μV offset," *IEEE J. Solid-State Circuits*, vol. 48, no. 12, pp. 3019–3027, Dec. 2013.

[45] R. T. Baird and T. S. Fiez, "Linearity enhancement of multibit $\Delta\Sigma$ A/D and D/A converters using data weighted averaging," *IEEE Trans. Circuits Syst. II, Analog Digit. Signal Process.*, vol. 42, no. 12, pp. 753–762, Dec. 1995.

[46] I. Galton, "Why dynamic-element-matching DACs work," *IEEE Trans. Circuits Syst. II, Exp. Briefs*, vol. 57, no. 2, pp. 69–74, Feb. 2010.

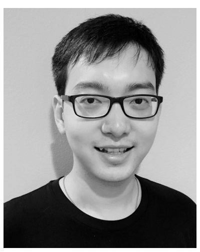

Xiahan Zhou (Member, IEEE) received the B.S. degree in electronic science and technology from the University of Electronic Science and Technology of China, Chengdu, China, in 2012, the M.S. degree (Hons.) in electrical engineering from the University of Southern California, Los Angeles, CA, USA, in 2014, and the Ph.D. degree in electrical and computer engineering from the University of California San Diego, La Jolla, CA, in 2020.

He is currently an Analog/Mixed-Signal Design Engineer with Qualcomm, Inc., San Diego, CA. His research interests are analog/mixed-signal circuits and systems for sensors and medical devices.

Dr. Zhou received the Qualcomm FMA Fellowship in 2017, the UCSD Geisel Fellowship in 2014, and the USC MS EE Honor in 2014.

Enhan Mai (Student Member, IEEE) received the B.S. degree (Hons.) in electrical engineering from the University of California Irvine, Irvine, CA, USA, in 2018, and the M.S. degree in electrical engineering from the University of California San Diego, La Jolla, CA, in 2020.

He is interested in RF/analog circuits.

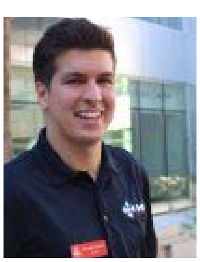

Michael Sveiven received the B.S. degree in biomedical engineering from the University of Arizona, Tucson, AZ, USA, in 2017.

He is currently working on point-of-care diagnostics for proteolytic diseases. His research focuses on the development of a point-of-care diagnostic device for rapid detection of proteases. He is currently optimizing surface chemistry techniques on magnetoresistive sensors to detect the presence of specific proteases often found in patients with cystic fibrosis, the most common, inherited fatal disease in Caucasians.

Corentin Pochet (Graduate Student Member, IEEE) received the B.S. and M.E. degrees in electrical engineering from the joint program between the Université Libre de Bruxelles (ULB), Brussels, Belgium, and the Vrije Universiteit Brussel (VUB), Brussels, in 2014 and 2016, respectively. He is currently pursuing the Ph.D. degree in electrical and computer engineering from the University of California San Diego (UCSD), San Diego, CA, USA.

His research interests include the design of low-power analog front-end circuits and time-based analog-to-digital converters for wearable and biomedical applications.

Mr. Pochet was a recipient of the Belgian American Education Foundation (B.A.E.F) Henri Benedictus Fellowship in 2016.

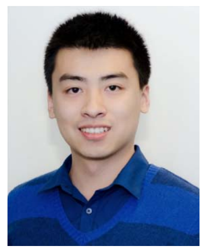

Haowei Jiang (Member, IEEE) received the B.S. degree in electrical engineering from the Huazhong University of Science and Technology (HUST), Wuhan, China, in 2014, and the M.S. and Ph.D. degrees in electrical and computer engineering from the University of California San Diego (UCSD), La Jolla, CA, USA, in 2016 and 2019, respectively.

He was an RF/analog design intern with Skyworks Inc., Newbury Park, CA, in 2018. He is currently an RF/analog design engineer with Apple Inc., San Diego, CA. His current research interests include the low-power wireless circuit design for the IoT applications and biomedical devices.

Dr. Jiang was a recipient of the IEEE Solid-State Circuits Society (SSCS) Predoctoral Achievement Award in 2019, the UCSD Geisel Fellowship in 2014, and the Chinese National Scholarship in 2011 and 2012.

Chih-Cheng Huang received the B.S. degree in materials science and engineering from National Taiwan University, Taipei, Taiwan, in 2010, the M.S. degree in nanoengineering from National Tsing Hua University, Hsinchu, Taiwan, in 2012, and the Ph.D. degree in materials science from the University of California San Diego, La Jolla, CA, USA, in 2020.

He is pursuing a career in management consulting. His research interests include nanomagnetism, PoC diagnostics, next-generation biosensing techniques, and proteomics.

Dr. Huang has been a member of the American Chemical Society (ACS) since 2012.

Drew A. Hall (Senior Member, IEEE) received the B.S. degree (Hons.) in computer engineering from the University of Nevada, Las Vegas, NV, USA, in 2005, and the M.S. and Ph.D. degrees in electrical engineering from Stanford University, Stanford, CA, USA, in 2008 and 2012, respectively.

From 2011 to 2013, he was a Research Scientist with the Integrated Biosensors Laboratory, Intel Corporation, Santa Clara, CA. Since 2013, he has been with the Department of Electrical and Computer Engineering, University of California San Diego, La Jolla, CA, where he is currently an Associate Professor. His research interests include bioelectronics, biosensors, analog circuit design, medical electronics, and sensor interfaces.

Dr. Hall won First Place in the Inaugural International IEEE Change the World Competition and First Place in the BME-IDEA invention competition, both in 2009. He received the Analog Devices Outstanding Designer Award in 2011, an Undergraduate Teaching Award in 2014, the Hellman Fellowship Award in 2014, an NSF CAREER Award in 2015, and an NIH Trailblazer Award in 2019. He is also a Tau Beta Pi Fellow. He has served as an Associate Editor of the IEEE TRANSACTIONS ON BIOMEDICAL INTEGRATED CIRCUITS since 2015 and a member of the CICC Technical Program Committee since 2017 and the ISSCC Technical Program Committee since 2020.